

Blowing Star Formation Away in AGN Hosts (BAH) - IV.

Serendipitous discovery of a $z \sim 2.9$ star-forming galaxy lensed by the galactic bulge of CGCG 012-070 using JWST NIRSpec

Rogemar A. Riffel^{1,2}, Carlos R. Melo-Carneiro³, Gabriel Luan Souza-Oliveira^{2,1}, Rogério Riffel³, Cristina Furlanetto⁴, Santiago Arribas¹, Marina Bianchin⁵, Ana L. Chies-Santos³, José Henrique Costa-Souza^{2,1}, Maitê S. Z. de Mellos², Michele Perna¹, Thaisa Storchi-Bergmann³, and Nadia L. Zakamska⁶

¹ Centro de Astrobiología (CAB), CSIC-INTA, Ctra. de Ajalvir km 4, Torrejón de Ardoz, E-28850, Madrid, Spain

² Departamento de Física, CCNE, Universidade Federal de Santa Maria, Av. Roraima 1000, 97105-900, Santa Maria, RS, Brazil

³ Departamento de Astronomia, IF, Universidade Federal do Rio Grande do Sul, CP 15051, 91501-970 Porto Alegre, RS, Brazil

⁴ Departamento de Física, IF, Universidade Federal do Rio Grande do Sul, CP 15051, 91501-970 Porto Alegre, RS, Brazil

⁵ Department of Physics and Astronomy, 4129 Frederick Reines Hall, University of California, Irvine, CA 92697, USA

⁶ Department of Physics & Astronomy, Johns Hopkins University, Bloomberg Ctr, 3400 N. Charles St, Baltimore, MD 21218, USA

Received September 15, 1996; accepted March 16, 1997

ABSTRACT

We report the detection of a gravitationally lensed galaxy by the nearby spiral galaxy CGCG 012-070 ($z = 0.048$) using Integral Field Unit (IFU) observations with the Near-Infrared Spectrograph (NIRSpec) instrument on board the James Webb Space Telescope (JWST). The lensed galaxy is identified through the flux distributions of emission lines in the rest-frame optical, consistent with a source located at a redshift of $z \sim 2.89$. The system is detected in [O III] $\lambda\lambda 4959, 5007$, H β , and H α emission lines, exhibiting line ratios typical of a star-forming galaxy. The emission-line flux distributions reveal three distinct components, which are modeled using an elliptical power-law (EPL) mass profile for the lens galaxy. This model provides a good characterization of the source and reveals a disturbed star-forming morphology consistent with those of galaxies at cosmic noon.

Key words. gravitational lensing: strong – galaxies: kinematics and dynamics – galaxies: spiral – galaxies: active

1. Introduction

Strong gravitational lensing occurs when the light from a distant background galaxy is distorted and magnified by the gravitational field of a foreground lens galaxy or galaxy cluster, aligned along the line of sight. This effect may produce multiple images or arcs of the background galaxy, with Einstein rings forming in cases of perfect alignment (e.g. Walsh et al. 1979; Saha et al. 2024). Strong gravitational lenses can provide valuable insights into the distribution of dark matter in galaxies and clusters (e.g. Tyson et al. 1998; Barnabè et al. 2012a), detection and characterization of high-redshift objects (e.g. Dye et al. 2018; Chirivi et al. 2020; Yue et al. 2023; Abdurro'uf et al. 2024), constrain cosmological parameters (e.g. Refsdal 1964; Shajib et al. 2020), and estimate the mass of supermassive black holes (e.g. Nightingale et al. 2023; Melo-Carneiro et al. 2025), among other applications.

The detection of strong gravitational lenses often involves several technical challenges, such as managing large imaging datasets and designing tools for precise identification (e.g. Metcalf et al. 2019). The number of identified gravitational lenses has been increasing rapidly due to the recent launch of the Euclid space telescope (Euclid Collaboration et al. 2024) and is expected to continue to grow, thanks to surveys such as the Legacy Survey of Space and Time (LSST; Ivezić et al. 2019). Gravitational lenses are found mainly in early-type galaxies, with only 10–20% in spirals (Auger et al. 2009), due to their lower mass and less concentrated mass distribution. Strong lenses pro-

duced by low-redshift spiral galaxies ($z \lesssim 0.1$) are even more uncommon (Treu et al. 2011; O’Riordan et al. 2025). Gravitational lenses in low-redshift galaxies are particularly insightful as the lensed arcs are observed in the central region of the galaxy, where the lensing primarily traces stellar mass. This, in turn, can be used as an independent constraint on the Initial Mass Function (IMF) mismatch parameter (e.g. Newman et al. 2017).

Here, we report the serendipitous detection of a strongly lensed galaxy by the spiral galaxy CGCG 012-070, located at $z = 0.048$, using observations taken with the Near-Infrared Spectrograph (NIRSpec) of the James Webb Space Telescope (JWST) in integral field unit (IFU) spectroscopy mode. This work is organized as follows: Section 2 describes the observations and the data reduction procedures, while Sec. 3 presents the results, which are discussed and summarized in Sec. 4.

2. Observations and data reduction

CGCG 012-070 is a nearly edge-on ($i \approx 70^\circ$) Sb galaxy and hosts a Seyfert 2 Active Galactic Nucleus (AGN; Kautsch et al. 2006; Véron-Cetty & Véron 2006). It was observed as part of the Blowing Star Formation Away in AGN Hosts (BAH; Costa-Souza et al. 2024; Riffel et al. 2025) project (PID: 1928, PI: Riffel, R. A.) using the JWST/NIRSpec instrument in the IFU mode (Böker et al. 2022). The observations were performed using the G235H filter in combination with the F170LP grating. We processed the data using the JWST Science Calibration Pipeline

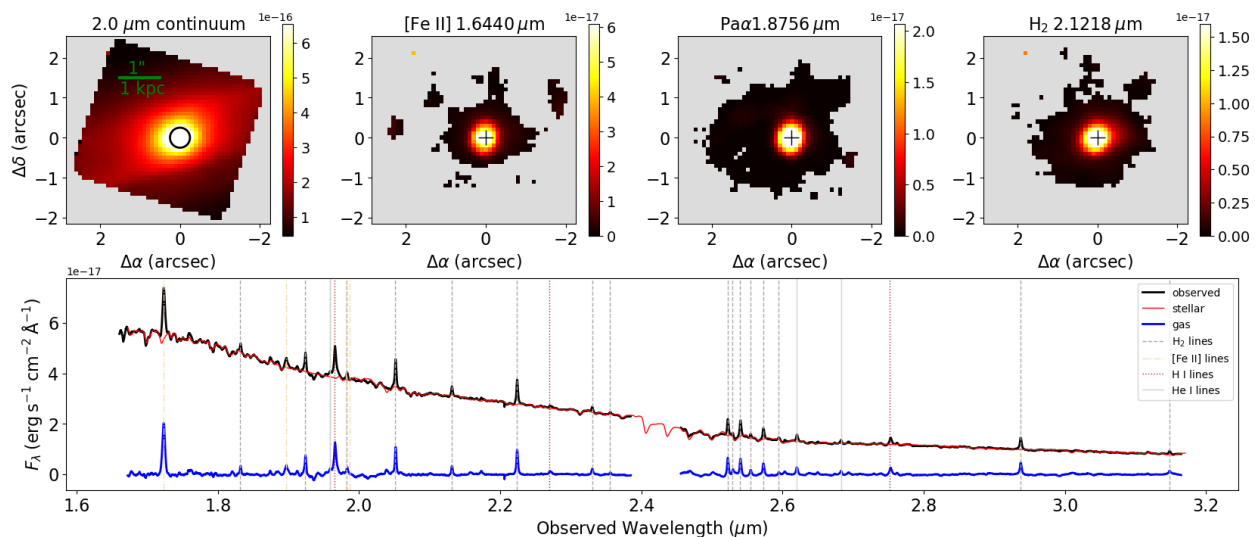


Fig. 1: **The CGCG 012-070 galaxy.** The top-left panel shows a $2.0\mu\text{m}$ continuum image of CGCG 012-070, obtained from the NIRSpc data cube. The other top panels display the flux distributions of the $[\text{Fe II}]$ $1.6440\mu\text{m}$, $\text{Pa}\alpha$, and H_2 $2.1218\mu\text{m}$ emission lines. Gray regions represent masked out areas where the $\text{snr} < 3$ and regions outside the NIRSpc FoV. The cross marks the position of the continuum peak. The bottom panel presents the observed spectrum (in black), integrated over a $0''.25$ radius nuclear aperture (black circle in the top-left panel). The red curve represents the stellar population (SP) model, while the blue curve shows the gas contribution (observed - SP). Vertical lines mark the position of the main emission lines.

(Bushouse et al. 2024), version 1.12.5, and the reference file `jwst_1183.pmap`, following the standard pipeline stages. See de Mellos et al. (2025) for details on observations and data processing.

3. Results

In Fig. 1, we present an image of the continuum at $2.0\mu\text{m}$ extracted from the NIRSpc data cube, along with flux maps for the $[\text{Fe II}]$ $1.6440\mu\text{m}$, $\text{Pa}\alpha$, and H_2 $2.1218\mu\text{m}$ emission lines. These maps were created by integrating the spectra over a 1500 km s^{-1} window centered on each emission line, after subtracting stellar population contribution obtained using the pPXF code (Cappellari 2023) in combination with the E-MILES templates (Vazdekis et al. 2016). The bottom panel shows the integrated nuclear spectrum integrated within a $0''.25$ radius aperture in black, while the underlying stellar continuum is shown in red and the gas emission spectrum is shown in blue. The continuum image follows the same orientation as the large-scale disc, elongated along position angle $\text{PA} \approx 107^\circ$ (Adelman-McCarthy et al. 2008). The emission-line flux distributions peak at the galaxy’s nucleus, with weaker extended emission detected up to $\sim 2''$ from it.

Through visual inspection of the NIRSpc data cube, we identified three components that are not associated with the galaxy but rather with a background object. These components are detected through the $\text{H}\beta$, $[\text{O III}] \lambda\lambda 4959, 5007$, and $\text{H}\alpha$ emission lines. The top panels of Fig. 2 display the observed flux distributions for $[\text{O III}] \lambda 5007$ and $\text{H}\alpha$, along with a composite image combining the $[\text{O III}] \lambda 5007$ emission (in red) and the continuum image of CGCG 012-070 (in green). The emission line maps were obtained by directly integrating the line profiles over velocity windows of 1500 km s^{-1} . Only spaxels where lines are detected with signal-to-noise $\text{snr} > 5$ are shown and components are labeled A, B, and C in the $[\text{O III}] \lambda 5007$ flux map. Component A exhibits an arc-shaped emission, whereas components B and C appear more point-like. The bottom panels of

Fig. 2 show the integrated spectra for each component. The insets in the spectra highlight the regions around the emission lines of the background object. The emission lines $[\text{Fe II}]$ $1.8298\mu\text{m}$ and H_2 $2.4237\mu\text{m}$, from the foreground galaxy, are also labeled. These emission lines do not affect the flux measurements of the background object’s lines, as they are outside the integration spectral windows.

The emission components of the background source closely resemble those of strong gravitational lenses observed in other galaxies (e.g. Treu et al. 2011; Galbany et al. 2018; Euclid Collaboration et al. 2025b,a), supporting their interpretation as such. Using the spectra of these components, we estimated the redshift for each one based on the emission lines. Using the $[\text{O III}] \lambda 5007$ line, we derive redshifts of 2.8871, 2.8869, and 2.8844 for components A, B, and C, respectively. Similarly, from the $\text{H}\alpha$ line, we estimate redshifts of 2.8872 and 2.8873 for components A and B. The mean redshift is $\langle z \rangle = 2.8866 \pm 0.0011$, where the uncertainty represents the standard deviation of the mean.

4. Discussions and Conclusions

Because of its prominence, we modelled the $[\text{O III}] \lambda 5007$ lensed emission using an elliptical power-law (EPL) mass profile for the lens galaxy, as implemented in PyAutoLens (Nightingale et al. 2018, 2021), and with the inclusion of an external shear. Before the modelling, we added background noise sampled from a normal distribution with a zero mean and a dispersion of $\sigma_{15} = 15\%$ of the peak arc brightness, in regions where there is no $[\text{O III}] \lambda 5007$ detection (Dutton et al. 2011; Barnabè et al. 2012b). Such noise is intended to suppress models that predict significant lensed features elsewhere. We assumed the uncertainty in this region to be equal to σ_{15} , and we estimated the uncertainty in the $[\text{O III}] \lambda 5007$ by assuming a Gaussian noise distribution. More details about the modelling strategy and systematic tests are presented in Appendix B.

Fig. 3 displays the highest-likelihood lens model, the normalised residuals, and the reconstructed $[\text{O III}] \lambda 5007$ source.

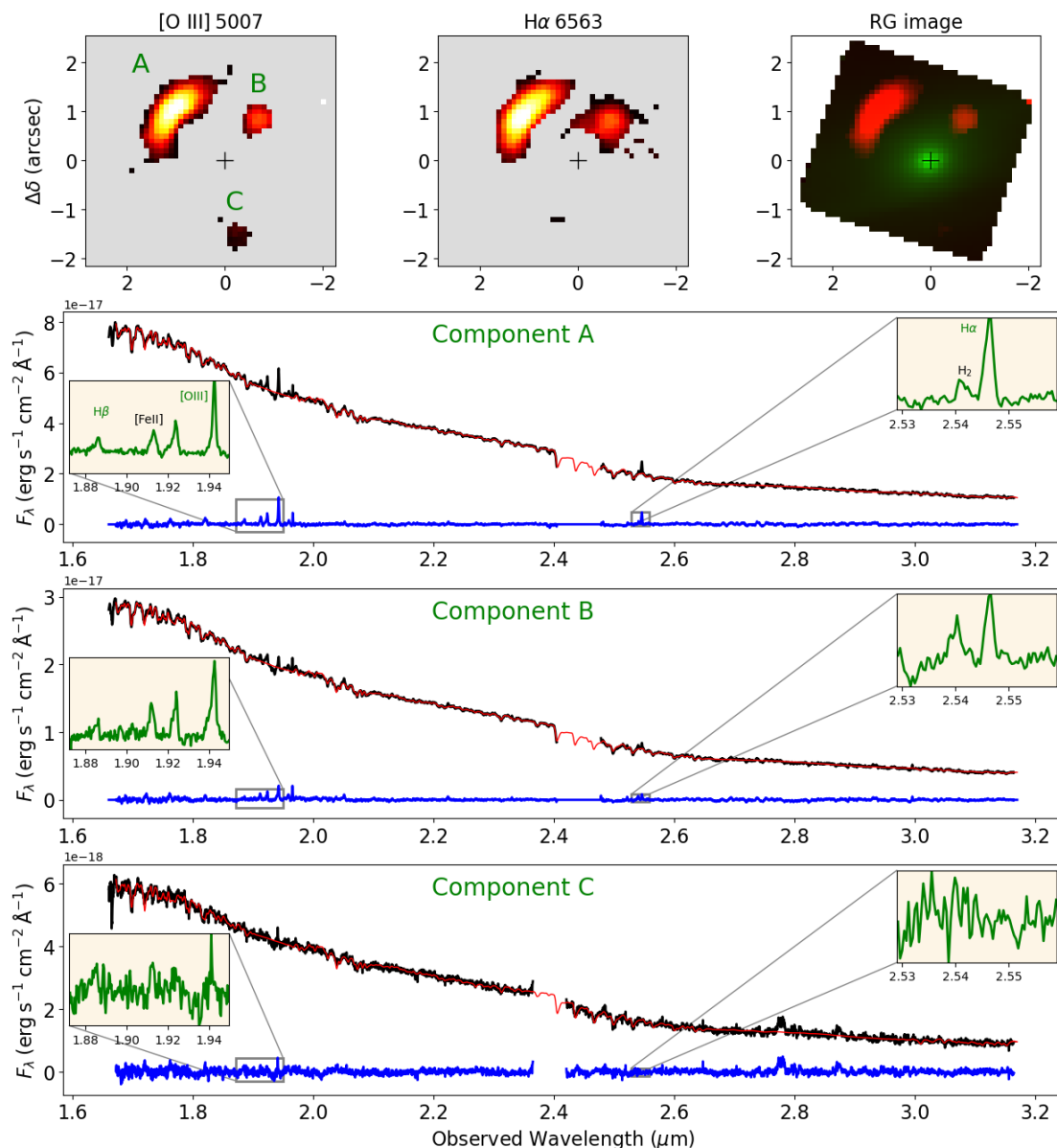


Fig. 2: **The lensed galaxy.** The top panels show the [O III] λ 5007 (left) and H α (center) flux maps for the $z \sim 2.89$ lensed object. The right panel presents a composite image, with the image of the lensed object shown in red and the 2.0 μ m continuum image of the galaxy CGCG 012-070 in green. The lower panels show the spectra at the positions of the lensed components A, B, and C, identified in the top-left panel. The observed spectra are shown in black, the stellar population contribution of CGCG 012-070 in red, and the gas component in blue. The insets provide a zoom-in on the [O III] and H α regions for the lensed object. The [Fe II] and H₂ labels, identified in black, represent Fe and H₂ lines from the foreground galaxy.

The model accurately fits the data, particularly component A, which exhibits a higher *snr*. We then used the same mask and mass model from this fit to reconstruct the H α emission, which we show in Fig. A.1. We found an effective Einstein radius for the EPL model, defined as the radius of a circle with the same area enclosed by the tangential critical curve, of $R_{\text{Ein}} = 1.75^{+0.03}_{-0.03}$ arcsec (~ 1.8 kpc), which corresponds to a total mass within it of $M_{\text{Ein}}(M_{\odot}/10^{10}) = 7.82^{+0.25}_{-0.31}$. This value is consistent with the one we estimate from stellar population synthesis for the lens galaxy, of $M_{\star}(M_{\odot}/10^{10}) = 6.88 \pm 0.89$, following Riffel et al. (2024). This results in an estimated dark matter fraction of $\sim 12\%$ within R_{Ein} , consistent with other low- z lens galaxies (e.g. Newman et al. 2017; Collett et al. 2018).

The reconstructed [O III] λ 5007 image has a disturbed morphology. Components A and B are traced to the same spatial location in the source plane, which indicates they correspond to an image and its counter-image. This interpretation is supported by the [O III] λ 5007 velocity measurements, which show similar values for these components. Component C is traced back to a different location in the source plane (white ellipse) and shows a [O III] λ 5007 velocity ~ 250 km s⁻¹ blueshifted relative to components A and B. Additionally, it is important to note that component C is unresolved and is detected only marginally. Despite tracing distinct galaxy components, such as gas rather than stars, this type of disturbed morphology is commonly observed in other lensed cosmic noon galaxies (Jones et al. 2010; Dye et al. 2015).

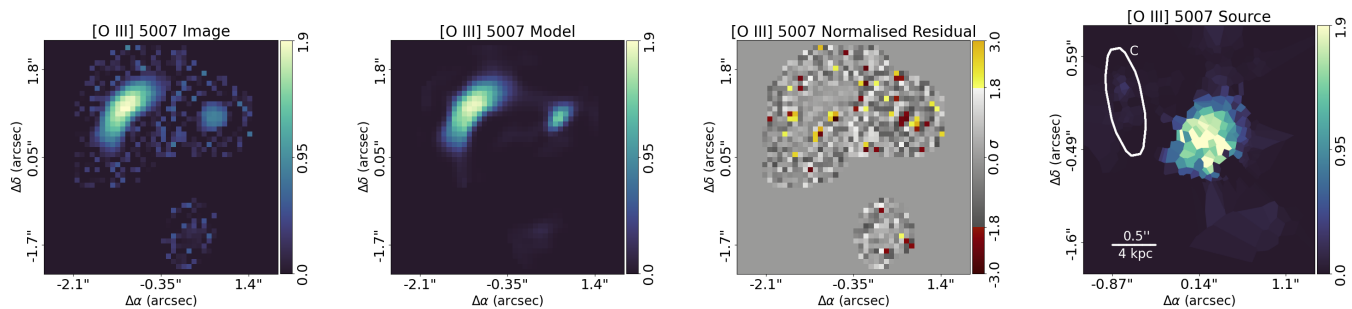


Fig. 3: Highest-likelihood EPL lens model for the [O III] $\lambda 5007$ emission. From left to right, we present the modified (noise-added) observed image, the model image, the normalised residuals, and the reconstructed source. Fluxes are in units of 10^{-18} erg s $^{-1}$ cm $^{-2}$.

Using the fluxes of the emission lines measured in an integrated spectrum, summing the components A and B, we obtain $\log [\text{O III}]\lambda 5007/\text{H}\beta = 0.71 \pm 0.08$. Although the [N II]6583 emission line is not detected, we can set an upper limit of $\log [\text{N II}]\lambda 6583/\text{H}\alpha < -1.1$. These values are consistent with emission originating from photoionization by young stars (Kewley et al. 2001; Kauffmann et al. 2003), indicating that the background object is a star-forming galaxy. This is also consistent with the disturbed morphology of the gas distribution in the reconstructed source, as discussed above. Using the [O III] velocity dispersion, of $\sigma \approx 120$ km s $^{-1}$ and a radius of 5 kpc, a rough estimate of the dynamical mass of the galaxy is $\log(M/M_{\odot}) \sim 10$. Using the H α luminosity, corrected for lensing magnification (factor of ~ 1.18), and the relation from Kennicutt (1998), we estimate a star formation rate of $\text{SFR} \sim 70 M_{\odot} \text{yr}^{-1}$, which is consistent with measurements reported for galaxies at similar redshifts (e.g., Förster Schreiber et al. 2009).

This work presents a remarkable discovery of a gravitational lens system with JWST, confirming the origin of its lensed [O III] $\lambda 5007$ and H α emissions. We estimate a redshift of $z \approx 2.89$ background source based on the central wavelengths of the observed emission lines. Additionally, the intensity ratios of these lines indicate that the primary ionization source of the gas is star formation. We modeled the lens system using an EPL profile, which effectively identified components A and B as a confirmed image and its counter-image. Furthermore, the model revealed a disturbed, star-forming source morphology consistent with cosmic noon galaxies. While our model provides a strong initial characterization, future deep imaging and spectroscopy will enable more detailed investigations of the lens and source objects, including constraining the IMF, but also will allow us to combine lens kinematics to precisely separate stellar and dark matter contributions within the lens galaxy.

Acknowledgements. RAR, GLSO, JHCS and MZM acknowledge the support from the Conselho Nacional de Desenvolvimento Científico e Tecnológico (CNPq; Projects 303450/2022-3, 403398/2023-1, and 441722/2023-7) and the Coordenação de Aperfeiçoamento de Pessoal de Nível Superior (CAPES; Project 88887.894973/2023-00, and Finance code 0001). RR acknowledges support from CNPq (Proj. 445231/2024-6, 311223/2020-6, 404238/2021-1, and 310413/2025-7), FAPERGS, (Proj. 19/1750-2 and 24/2551-0001282-6) and CAPES (88881.109987/2025-01). CF acknowledges the support from CNPq Project 315421/2023-1

References

Abdurro'uf, Larson, R. L., Coe, D., et al. 2024, *ApJ*, 973, 47
 Adelman-McCarthy, J. K., Agüeros, M. A., Allam, S. S., et al. 2008, *ApJS*, 175, 297
 Auger, M. W., Treu, T., Bolton, A. S., et al. 2009, *ApJ*, 705, 1099

Barnabè, M., Dutton, A. A., Marshall, P. J., et al. 2012a, *MNRAS*, 423, 1073
 Barnabè, M., Dutton, A. A., Marshall, P. J., et al. 2012b, *MNRAS*, 423, 1073
 Böker, T., Arribas, S., Lützgendorf, N., et al. 2022, *A&A*, 661, A82
 Collett, T. E., Oldham, L. J., Smith, R. J., et al. 2018, *Science*, 360, 1342
 Costa-Souza, J. H., Riffel, R. A., Souza-Oliveira, G. L., et al. 2024, *ApJ*, 974, 127
 de Mello, M. S. Z., Riffel, R. A., Souza-Oliveira, G. L., et al. 2025, *arXiv e-prints*, arXiv:2506.20896
 Dutton, A. A., Brewer, B. J., Marshall, P. J., et al. 2011, *MNRAS*, 417, 1621
 Dye, S., Furlanetto, C., Dunne, L., et al. 2018, *MNRAS*, 476, 4383
 Dye, S., Furlanetto, C., Swinbank, A. M., et al. 2015, *MNRAS*, 452, 2258
 Etherington, A., Nightingale, J. W., Massey, R., et al. 2022, *MNRAS*, 517, 3275
 Euclid Collaboration, Mellier, Y., Abdurro'uf, et al. 2024, *arXiv e-prints*, arXiv:2405.13491
 Euclid Collaboration, Rojas, K., Collett, T. E., et al. 2025a, *arXiv e-prints*, arXiv:2503.15325
 Euclid Collaboration, Walmsley, M., Holloway, P., et al. 2025b, *arXiv e-prints*, arXiv:2503.15324
 Förster Schreiber, N. M., Genzel, R., Bouché, N., et al. 2009, *ApJ*, 706, 1364
 Galbany, L., Collett, T. E., Méndez-Abreu, J., et al. 2018, *MNRAS*, 479, 262
 Ivezić, Z., Kahn, S. M., Tyson, J. A., et al. 2019, *ApJ*, 873, 111
 Jones, T. A., Swinbank, A. M., Ellis, R. S., Richard, J., & Stark, D. P. 2010, *MNRAS*, 404, 1247
 Kauffmann, G., Heckman, T. M., Tremonti, C., et al. 2003, *MNRAS*, 346, 1055
 Kautsch, S. J., Grebel, E. K., Barazza, F. D., & Gallagher, J. S., I. 2006, *A&A*, 445, 765
 Kennicutt, Jr., R. C. 1998, *ARA&A*, 36, 189
 Kewley, L. J., Dopita, M. A., Sutherland, R. S., Heisler, C. A., & Trevena, J. 2001, *ApJ*, 556, 121
 Melo-Carneiro, C. R., Furlanetto, C., & Chies-Santos, A. L. 2025, *J. Cosmology Astropart. Phys.*, 2025, 046
 Meneghetti, M., Bartelmann, M., Dahle, H., & Limousin, M. 2013, *Space Sci. Rev.*, 177, 31
 Metcalf, R. B., Meneghetti, M., Avestruz, C., et al. 2019, *A&A*, 625, A119
 Newman, A. B., Smith, R. J., Conroy, C., Villaume, A., & van Dokkum, P. 2017, *ApJ*, 845, 157
 Nightingale, J., Hayes, R., Kelly, A., et al. 2021, *The Journal of Open Source Software*, 6, 2825
 Nightingale, J. W., Dye, S., & Massey, R. J. 2018, *MNRAS*, 478, 4738
 Nightingale, J. W., Smith, R. J., He, Q., et al. 2023, *MNRAS*, 521, 3298
 O'Riordan, C. M., Oldham, L. J., Nersesian, A., et al. 2025, *A&A*, 694, A145
 Planck Collaboration, Ade, P. A. R., Aghanim, N., et al. 2016, *A&A*, 594, A13
 Refsdal, S. 1964, *MNRAS*, 128, 307
 Riffel, R., Dahmer-Hahn, L. G., Vazdekis, A., et al. 2024, *MNRAS*, 531, 554
 Riffel, R. A., Souza-Oliveira, G. L., Costa-Souza, J. H., et al. 2025, *ApJ*, 982, 69
 Saha, P., Sluse, D., Wagner, J., & Williams, L. L. R. 2024, *Space Sci. Rev.*, 220, 12
 Shajib, A. J., Birrer, S., Treu, T., et al. 2020, *MNRAS*, 494, 6072
 Sibson, R. 1981, in *Interpreting Multivariate Data*, ed. V. Barnett (New York: John Wiley & Sons), 21–36
 Speagle, J. S. 2020, *MNRAS*, 493, 3132
 Tessore, N. & Metcalf, R. B. 2015, *A&A*, 580, A79
 Treu, T., Dutton, A. A., Auger, M. W., et al. 2011, *MNRAS*, 417, 1601
 Tyson, J. A., Kochanski, G. P., & Dell'Antonio, I. P. 1998, *ApJ*, 498, L107
 Vazdekis, A., Koleva, M., Ricciardelli, E., Röck, B., & Falcón-Barroso, J. 2016, *MNRAS*, 463, 3409–3436
 Véron-Cetty, M. P. & Véron, P. 2006, *A&A*, 455, 773
 Walsh, D., Carswell, R. F., & Weymann, R. J. 1979, *Nature*, 279, 381
 Yue, M., Fan, X., Yang, J., & Wang, F. 2023, *AJ*, 165, 191

Appendix A: H α reconstructed image

Fig. A.1 shows the results of the EPL lens model for the H α flux distribution, using the same mask and mass model derived for the [O III] λ 5007 emission¹.

Appendix B: Some details of the lens modeling

We performed the modelling using the open source lens modelling package PyAutoLens (Nightingale et al. 2018). Our approach utilized the SLAM (Source, Light, and Mass) pipelines distributed with PyAutoLens, similar to the methods employed in other works (e.g., Cao et al. 2022; Etherington et al. 2022), but with modifications to match our data. The pipeline workflow is summarized below:

- 1. Initialize:** We began by creating a basic model for the lens mass and source light distribution using parametric profiles. The lens mass is assumed to be a singular isothermal ellipsoid (SIE)+shear, and the source's brightness was modeled by a Sersic component.
- 2. Lens Refinement and Source Pixelization:** Using the results from the initial step, we re-sampled the lens mass model parameters alongside a pixelized source model. We employed a Voronoi mesh grid with Natural Neighbor interpolation (Sibson 1981) and brightness-adaptive regularization to smooth the reconstruction based on source luminosity. Priors on the mass parameters were updated using PyAutoLens's default prior passing².
- 3. Source Pixelization Refinement:** We refined the source plane reconstruction using the results from the previous phase. The mass model was fixed to its highest-likelihood parameters, while the source plane parameters were re-sampled. The source was reconstructed using a brightness-adaptive Voronoi mesh grid with Natural Neighbor interpolation and brightness-adaptive regularization. In PyAutoLens notation, this corresponds to a KMeans mesh grid, with VoronoiNN pixelization, and AdaptiveBrightnessSplit regularization. During this reconstruction, we fixed the number of KMeans clusters to 500.
- 4. Lens Mass Refinement:** With the source reconstruction fixed to the highest-likelihood model from the previous step, we refined the mass model. The lens mass profile was updated to an EPL + shear, allowing for greater complexity. Again, the priors are updated using the default prior passing from PyAutoLens.

This pipeline concludes with the fitting of the EPL+shear model, which is the final model used for the analysis presented in this work. The convergence of the EPL mass profile is given by (Tessore & Metcalf 2015):

$$\kappa(\xi) = \frac{(3 - \gamma^{\text{lens}})}{1 + q^{\text{lens}}} \left(\frac{\theta_{\text{Ein}}^{\text{lens}}}{\xi} \right)^{\gamma^{\text{lens}} - 1}. \quad (\text{B.1})$$

Here, q^{lens} is the axis ratio (minor-to-major axis), and ξ is the elliptical coordinate, defined as $\xi = \sqrt{x^2 + (y/q^{\text{lens}})^2}$. The parameter $\theta_{\text{Ein}}^{\text{lens}}$ is Einstein radius in units of arcsec, and γ^{lens} is the mass density slope; this profile reduces to a SIE when $\gamma^{\text{lens}} = 2$.

¹ For this purpose, we kept the mass model fixed and sampled only the source-plane pixelization and regularization parameters.

² Additional details are available in the online documentation for PyAutoLens: https://github.com/Jammy2211/autolens_workspace.

Table B.1: Inferred median and 1σ credible intervals for model parameters. Parameters are, in order, lens potential centre (x_0, y_0) , lens mass elliptical components (ϵ_1, ϵ_2) , EPL Einstein radius $\theta_{\text{Ein}}^{\text{lens}}$, EPL density slope γ^{lens} , elliptical shear components $(\epsilon_1^{\text{sh}}, \epsilon_2^{\text{sh}})$, effective Einstein radius R_{Ein} , and the total mass within it M_{Ein} . Columns represent individual datasets or models (refer to text for details).

Parameter	Model σ_{10}	Model σ_{15} (fiducial)	Model σ_{20}
x_0 ["]	$-0.05^{+0.01}_{-0.01}$	$-0.05^{+0.01}_{-0.01}$	$-0.03^{+0.01}_{-0.01}$
y_0 ["]	$-0.10^{+0.01}_{-0.02}$	$-0.14^{+0.02}_{-0.03}$	$-0.19^{+0.03}_{-0.03}$
ϵ_1	$0.75^{+0.01}_{-0.01}$	$0.74^{+0.02}_{-0.02}$	$0.68^{+0.02}_{-0.02}$
ϵ_2	$-0.07^{+0.01}_{-0.02}$	$-0.10^{+0.03}_{-0.03}$	$-0.16^{+0.04}_{-0.04}$
$\theta_{\text{Ein}}^{\text{lens}}$ ["]	$3.00^{+0.11}_{-0.10}$	$2.97^{+0.16}_{-0.13}$	$2.69^{+0.10}_{-0.09}$
γ^{lens}	$2.19^{+0.03}_{-0.04}$	$2.27^{+0.03}_{-0.04}$	$2.37^{+0.04}_{+0.04}$
ϵ_1^{sh}	$-0.09^{+0.02}_{-0.01}$	$-0.06^{+0.01}_{-0.01}$	$-0.07^{+0.01}_{+0.01}$
ϵ_2^{sh}	$-0.04^{+0.03}_{-0.02}$	$-0.12^{+0.03}_{-0.02}$	$-0.18^{+0.02}_{-0.02}$
R_{Ein} ["]	$1.76^{+0.02}_{-0.02}$	$1.75^{+0.03}_{-0.03}$	$1.67^{+0.03}_{-0.04}$
$M_{\text{Ein}}[M_{\odot}/10^{10}]$	$7.85^{+0.22}_{-0.16}$	$7.82^{+0.25}_{-0.31}$	$7.09^{+0.23}_{-0.30}$

Additionally, the mass position angle, ϕ^{lens} , measured counter-clockwise from the positive x -axis, can be incorporated using the elliptical components:

$$\epsilon_1 = \frac{1 - q^{\text{lens}}}{1 + q^{\text{lens}}} \sin 2\phi^{\text{lens}}, \quad \epsilon_2 = \frac{1 - q^{\text{lens}}}{1 + q^{\text{lens}}} \cos 2\phi^{\text{lens}}. \quad (\text{B.2})$$

It is worth mentioning that the Einstein radius $\theta_{\text{Ein}}^{\text{lens}}$ in this equation differs from the *effective* Einstein radius as defined by Meneghetti et al. (2013). The *effective* Einstein radius, which is the one applied in our analysis, corresponds to the radius of a circle having the same area as the region enclosed by the tangential critical curve.

The lensing external shear is parametrized by its elliptical components, $(\epsilon_1^{\text{sh}}, \epsilon_2^{\text{sh}})$, as follows:

$$\gamma^{\text{sh}} = \sqrt{\epsilon_1^{\text{sh}2} + \epsilon_2^{\text{sh}2}}, \quad \tan(2\phi^{\text{sh}}) = \frac{\epsilon_2^{\text{sh}}}{\epsilon_1^{\text{sh}}}, \quad (\text{B.3})$$

where γ^{sh} and ϕ^{sh} are the shear amplitude and shear angle, measured counter-clockwise from north, respectively.

We performed the sampling using the nested sampler dynesty (Speagle 2020). When necessary, we adopted a cosmology consistent with Planck Collaboration et al. (2016). The median of each parameter's one-dimensional marginalized posterior distribution, along with uncertainties corresponding to the 16th and 84th percentiles for our models, are presented in Table B.1.

We investigated the impact of the introduced noise level on empty regions on our modeling results. While our fiducial model assumes a dispersion of $\sigma_{15} = 15\%$ of the peak arc brightness for the introduced noise, we performed additional tests using dispersion values of σ_{10} and σ_{20} . The results of these alternative

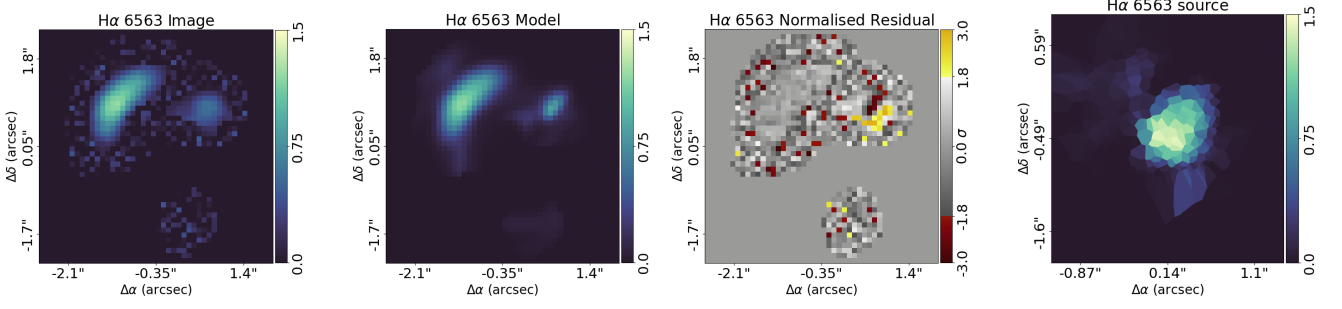


Fig. A.1: $H\alpha$ reconstruction, utilizing the mass model obtained from fitting the $[O\text{ III}] \lambda 5007$ emission. From left to right, we present the modified (noise-added) observed image, the model image, the normalised residuals, and the reconstructed source. Fluxes are in units of $10^{-18} \text{ erg s}^{-1} \text{ cm}^{-2}$.

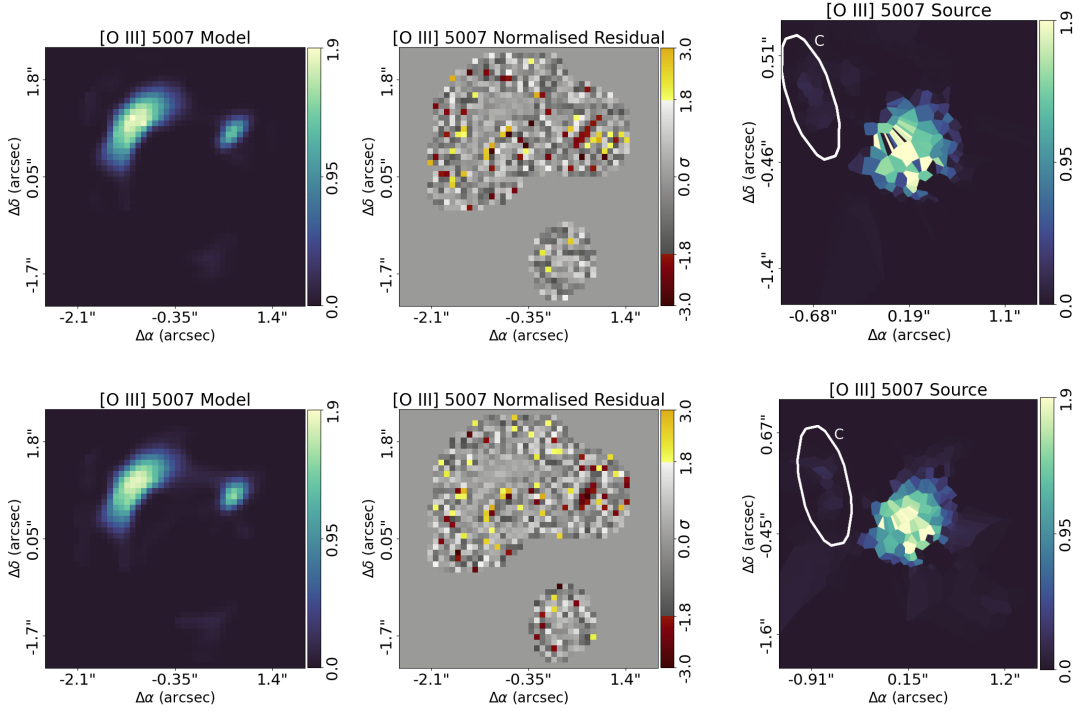


Fig. A.2: Highest-Likelihood EPL Lens Models for Alternative Datasets. Each row illustrates a different assumption for the noise added to empty regions. From left to right, we present the model image, normalized residuals, and reconstructed source. The top row shows the dataset where the modified image uses a σ_{10} dispersion, while the bottom row corresponds to a σ_{20} dispersion. Fluxes are in units of $10^{-18} \text{ erg s}^{-1} \text{ cm}^{-2}$.

datasets are presented in Fig. A.2, with the median posterior distributions of the parameters detailed in Table B.1. Overall, our results demonstrate consistency across the tested noise levels, but we found that the data were best fitted when a dispersion of σ_{15} was applied (see the normalized residual maps at the B region).